

NO₂ air afterglow and O and NO densities from Odin-OSIRIS night and ACE-FTS sunset observations in the Antarctic MLT region

R. L. Gattinger,¹ I. C. McDade,² A. L. Alfaro Suzán,² C. D. Boone,³ K. A. Walker,^{3,4} P. F. Bernath,^{3,5} W. F. J. Evans,² D. A. Degenstein,¹ J.-H. Yee,⁶ P. Sheese,^{1,2} and E. J. Llewellyn¹

Received 14 September 2009; revised 18 February 2010; accepted 2 March 2010; published 16 June 2010.

[1] The continuum spectrum produced by the NO + O(+M) → NO₂(+M) + *hν* chemiluminescent reaction has been detected in the upper mesospheric dark polar regions by Optical Spectrograph and Infra-Red Imager System (OSIRIS) on the Odin spacecraft. For the sample period of 8–9 May 2005, Southern Hemisphere, limb radiance profiles of continuum spectra, resolved from OH airglow and auroral contamination, are inverted to obtain volume emission rate altitude profiles. The maximum observed differential brightness referred to zenith viewing is 1.2×10^7 photons cm⁻² s⁻¹ nm⁻¹ at 580 nm with a measurement uncertainty 5×10^5 photons cm⁻² s⁻¹ nm⁻¹, for an analysis range 80–101 km. Atomic oxygen densities [O] required by the analysis to derive NO densities [NO] are determined from OSIRIS O₂(b¹Σ_g⁺ – X³Σ_g⁻) 0-0 band night airglow observations and from Atmospheric Chemistry Experiment-Fourier Transform Spectrometer (ACE-FTS) sunset ozone observations. The derived Southern Hemisphere [O] map that shows pronounced longitudinal variation, maximum of 7×10^{11} cm⁻³, considerably exceeding MSIS model values, and suggests significant dynamical influence. Combining the continuum observations and the derived [O], a hemispheric map of derived [NO] is assembled that also shows considerable spatial variation, maximum of 1.1×10^9 cm⁻³, measurement uncertainty of 3×10^7 cm⁻³. Comparing the two maps, the geographical distribution of [NO] differs considerably from that of [O]. From a qualitative comparison, the distribution of derived [NO] is similar to that in coordinated GUVI LBH1 auroral precipitation images. The OSIRIS-derived [NO] agrees with the measured ACE-FTS [NO] to within 1×10^8 cm⁻³. The estimated systematic uncertainty of the NO densities derived from OSIRIS observations is approximately 30%.

Citation: Gattinger, R. L., et al. (2010), NO₂ air afterglow and O and NO densities from Odin-OSIRIS night and ACE-FTS sunset observations in the Antarctic MLT region, *J. Geophys. Res.*, 115, D12301, doi:10.1029/2009JD013205.

1. Introduction

[2] Thermospheric NO_x [NO + NO₂] can be transported down to the lower mesosphere and stratosphere by meridional circulation during the polar winter without being

photochemically destroyed [e.g., *Solomon et al.*, 1982; *Russell et al.*, 1984; *Siskind et al.*, 2000]. More recent observations of NO_x transport include those by *Funke et al.* [2005] from MIPAS measurements, *Randall et al.* [2006] with Atmospheric Chemistry Experiment-Fourier Transform Spectrometer (ACE-FTS) solar occultation observations, and *Hauchecorne et al.* [2007] with GOMOS and SABER data. In the stratosphere NO_x is part of the NO_y budget and plays a role in catalytic loss of O₃ [e.g., *Jucks et al.*, 1996]. *Vogel et al.* [2008] have estimated an O₃ vertical column loss of approximately 3% from downward transported thermospheric NO_x during winters with unusual dynamic conditions.

[3] Global spatial and temporal distributions of thermospheric NO observed by the SNOE instrument, measuring fluorescent scattering of ultraviolet solar radiation by nitric oxide, have been summarized by *Barth et al.* [2003]. Lower thermospheric NO_x originates predominantly with solar soft

¹Department of Physics and Engineering Physics, University of Saskatchewan, Saskatoon, Saskatchewan, Canada.

²Centre for Research in Earth and Space Science (CRESS) and Department of Earth and Space Science and Engineering (ESSE), York University, Toronto, Ontario, Canada.

³Department of Chemistry, University of Waterloo, Waterloo, Ontario, Canada.

⁴Department of Physics, University of Toronto, Toronto, Ontario, Canada.

⁵Department of Chemistry, University of York, Heslington, York, UK.

⁶Johns Hopkins University Applied Physics Laboratory, Laurel, Maryland, USA.

X-ray radiance at low latitudes in the daytime and with auroral particles at high latitudes [Bailey *et al.*, 2002]. However, the SNOE observations do not cover thermospheric NO_x in the dark polar regions, which potentially play a role in stratospheric ozone chemistry.

[4] The primary objective of the current study is to assess the feasibility of measuring NO_x densities in the dark polar regions of the upper mesosphere and lower thermosphere (MLT) with the Optical Spectrograph and Infra-Red Imager System (OSIRIS) [Llewellyn *et al.*, 2004] on the Odin spacecraft [Murtagh *et al.*, 2002]. The ability to measure NO_x in the absence of sunlight will potentially assist in quantifying the relative importance of the MLT source of NO_x in stratospheric photochemistry. The technique is based on observing the yellow-green air afterglow continuum produced in the reaction $\text{NO} + \text{O}(+M) \rightarrow \text{NO}_2^*(+M) + h\nu$ [Stewart, 1957]. Note that very little NO_x in the MLT is held in the form of NO₂ due to the efficiency of the $\text{NO}_2 + \text{O} \rightarrow \text{NO} + \text{O}_2$ reaction. There have been a number of previous observations of this chemiluminescent continuum, Sharp [1978] and Witt *et al.* [1981] at high latitudes and McDade *et al.* [1986a] and von Savigny *et al.* [1999] at middle and low latitudes. For this introductory study of the OSIRIS NO₂ continuum, observations have been confined to the period 8–9 May 2005 in the Southern Hemisphere.

[5] The procedures for obtaining altitude profiles of the NO₂ continuum limb radiances from the OSIRIS spectra are discussed in section 2. The continuum volume emission rate (VER) altitude profiles are then calculated. A Southern Hemisphere map of the vertically integrated VER is included.

[6] To obtain NO densities [NO] from the air afterglow reaction, the analysis relies critically on a knowledge of the atomic oxygen density [O]. In previous experiments [e.g., McDade *et al.*, 1986b], [O] was either inferred or measured directly. Because of the very dynamic nature of the MLT region [e.g., Winick *et al.*, 2009], it is advantageous to measure [O] and the NO₂ air afterglow at the same location and time. For the current analysis, [O] is inferred from concurrent OSIRIS spectral observations of the O₂(b¹Σ_g⁺ – X³Σ_g⁻) 0–0 band, following the method developed by McDade *et al.* [1986b]. The procedures are described in section 3. The absolute accuracy of [O] derived from the OSIRIS observations is tested against [O] derived from coordinated Atmospheric Chemistry Experiment–Fourier Transform Spectrometer (ACE–FTS) [Bernath *et al.*, 2005] sunset ozone observations. The results are compared with predicted [O] distributions from the MSIS model [Picone *et al.*, 2002]. A Southern Hemisphere map of [O] is included to demonstrate the observed spatial distribution.

[7] The procedures for obtaining [NO] from the derived [O] altitude profiles and the measured NO₂ continuum VER profiles are described in section 4. The analysis requires knowledge of the spectral distribution and absolute emission efficiency the NO₂ afterglow continuum, available from laboratory measurements by Becker *et al.* [1972] and Whytock *et al.* [1976]. Gattinger *et al.* [2009] updated the spectral distribution by direct measurements in the MLT region. Again, a Southern Hemisphere map of [NO] is included to demonstrate the observed spatial distribution. The derived OSIRIS [NO] values are compared with the longitudinal distribution of coordinated ACE–FTS sunset [NO] measurements in section 5.

[8] Finally, the observations are briefly discussed in section 6 with emphasis on the observed spatial variability of the three components, NO₂ continuum VER, [O], and [NO], and possible source mechanisms.

2. The OSIRIS NO₂ Continuum Observations

[9] The OSIRIS observations presented here are limited to emissions measured in the Southern Hemisphere night, so differing from previous OSIRIS observations of limb-scattered solar radiation [e.g., Gattinger *et al.*, 2006]. The full spectral range of the spectrograph is from 275 to 810 nm with a data gap between 480 and 530 nm due to the spectral order sorter. The wavelength sampling interval is 0.4 nm, and the spectral slit width is approximately 0.9 nm. The vertical field of view is 1 km at the limb tangent point, and the absolute limb pointing knowledge is approximately 0.5 km. The limb scan rate is 0.75 km s⁻¹, and at mesospheric altitudes the exposure time varies between 1 and 2 s for the period included in this analysis. The prelaunch absolute spectral response was determined using standard lamps, followed by on-orbit calibrations using stars. Absolute response changes throughout the mission are tracked by comparison with a three-dimensional limb radiance forward model [Bourassa *et al.*, 2008] with an estimated absolute accuracy of ±10% and relative spectral accuracy of ±5%.

[10] As described by Gattinger *et al.* [2009], a reference spectral profile of the NO₂ emission continuum has been obtained from the OSIRIS data set. The spectral profile, corresponding to mesopause region atmospheric pressure, is slightly different from the low-pressure spectral shape measured in the laboratory by Becker *et al.* [1972]. The shortwave limit of the continuum is approximately 370 nm in agreement with the measurements by Stewart [1957]. This spectral profile, obtained using the OSIRIS data, is assumed throughout the analysis.

[11] Using the technique described by Gattinger *et al.* [2009] the reference NO₂ emission continuum and the reference OH airglow spectrum are simultaneously fit to the total observed limb spectrum, interpolated to 1 km altitude intervals, to isolate the NO₂ component. Examples of OSIRIS limb radiance spectra at 88 km limb tangent altitude are shown in Figure 1, one case is for the bright NO₂ continuum typically found within the dark polar region (Figure 1a) and the other is for the normally faint emission found at mid-latitude (Figure 1b). Both cases are from 9 May 2005, at approximately 19 local solar time (LST) and are at similar longitudes. The spectral fitting range is limited to 430–710 nm, the brighter section of the NO₂ continuum. Within that range, the auroral 558 nm OI line and the 660–680 nm N₂ first positive bands are excluded in order to reduce the impact of auroral contamination. The spectral region from 710 to 810 nm is also excluded because of possible contamination by auroral emissions, including both the N₂ first positive and N₂⁺ Meinel bands [Vallance Jones, 1974]. Also, because the OH vibration-rotation bands above 710 nm are considerably brighter than those below 710 nm (Figure 1b), the uncertainty in the fitting process would be increased if the region above 710 nm were included. It should be noted that the region below 430 nm is also excluded because of possible contamination from strong auroral emissions, e.g., the N₂⁺ 0–1 first negative band at 428 nm.

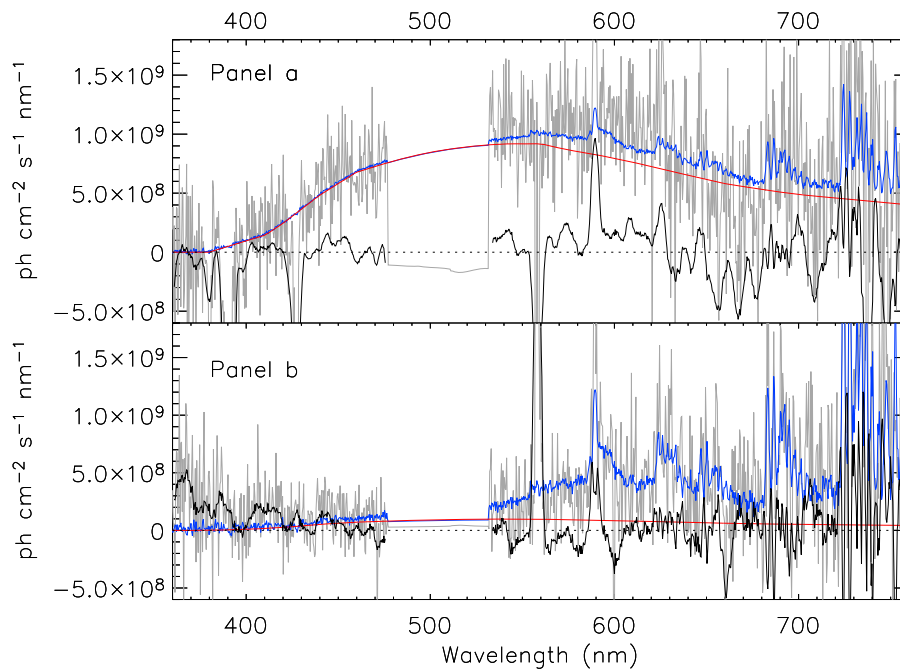


Figure 1. Limb radiance spectra observed by OSIRIS at 88 km tangent altitude, 9 May 2005. (a) From the dark polar region (75°S, 225°E) with enhanced NO₂ continuum radiance. (b) Midlatitude (29°S, 221°E) with very little NO₂ continuum. Gray, observed limb spectrum; blue, least squares fit of sum of scaled night airglow and scaled NO₂ continuum spectra; black, residual of gray minus blue components, smoothed to improve clarity; red, derived NO₂ continuum at 88 km limb.

[12] In general, because the CCD detector dark pattern is obtained by averaging a number of limb spectra at approximately 110 km tangent altitude, the dark pattern will include any auroral component that might be present at that altitude. Since auroral excitation does not normally penetrate below approximately 100 km [Vallance Jones, 1974], when the CCD dark pattern is subtracted from each limb spectrum in the 80–100 km region, the subtracted auroral component can at times result in a negative signal (e.g., Figure 1a).

[13] The residual spectra in Figures 1a and 1b are obtained by subtracting from the observed limb spectrum the sum of the scaled NO₂ continuum reference and the scaled OH airglow reference. Spectral smoothing with an arbitrary 4 nm triangular function has been applied to the residual spectra to improve plot clarity. For the unsmoothed residual spectrum the standard deviation for individual pixels is typically less than 4×10^8 photons cm⁻² s⁻¹ nm⁻¹. Applying the fitting procedure over the broad spectral range from 430 to 710 nm reduces the NO₂ continuum measurement uncertainty by a factor of approximately 20 to typically 2×10^7 photons cm⁻² s⁻¹ nm⁻¹. This noise floor is determined mainly by detector and readout noise and is thus largely altitude independent.

[14] The above spectral fitting procedure is repeated for each of the limb spectra, interpolated to a 1 km tangent limb grid, and plotted as NO₂ continuum limb radiance profiles in Figure 2. These profiles are expressed in units of spectral differential brightness at 580 nm, the spectral peak of the NO₂ continuum. For the period 8–9 May 2005, the limb scans extend to above 110 km and so make it possible to process the limb data up to approximately 100 km. Measurement errors, typically 2×10^7 photons cm⁻² s⁻¹ nm⁻¹ as

stated above, are calculated at 1 km intervals based on the residuals and plotted at 4 km intervals. From Figure 1, the difference between the NO₂ continuum brightness typically seen in the predominantly dark polar region and in the midlatitude region is readily apparent.

[15] It should be noted that the averaged low-latitude OH night airglow continuum used in the spectral fitting procedure itself contains a weak underlying NO₂ continuum [e.g., Broadfoot and Kendall, 1968]. This leads to an NO₂ continuum overcorrection of approximately 4×10^7 photons cm⁻² s⁻¹ nm⁻¹ when referred to the limb radiance values in Figure 2 or twice the measurement error. At altitudes above 95 km, this effect is considerably smaller due to the decrease in the OH emission brightness with increasing altitude. The relative importance of this systematic effect is discussed in the following sections.

[16] The VER profiles derived by inverting the NO₂ continuum limb radiance profiles in Figure 2 are shown in Figure 3. When using NO₂ continuum VER profiles to derive [NO], discussed in a later section, the sum of the differential brightness over all wavelengths from 370 to 1400 nm [Becker et al., 1972] is required. To this end the units in Figure 3 have been converted from spectral differential brightness to total continuum brightness by multiplying the measured 580 nm peak differential brightness of the NO₂ continuum by the 450 nm equivalent spectral width of the total continuum [Becker et al., 1972]. The computed VER profiles are smoothed with a 7 km triangular function before plotting. Measurement errors in the smoothed NO₂ continuum VER profiles are typically less than 200 photons cm⁻³ s⁻¹ (Table 1). This measurement error in VER is propagated in the analysis from the NO₂

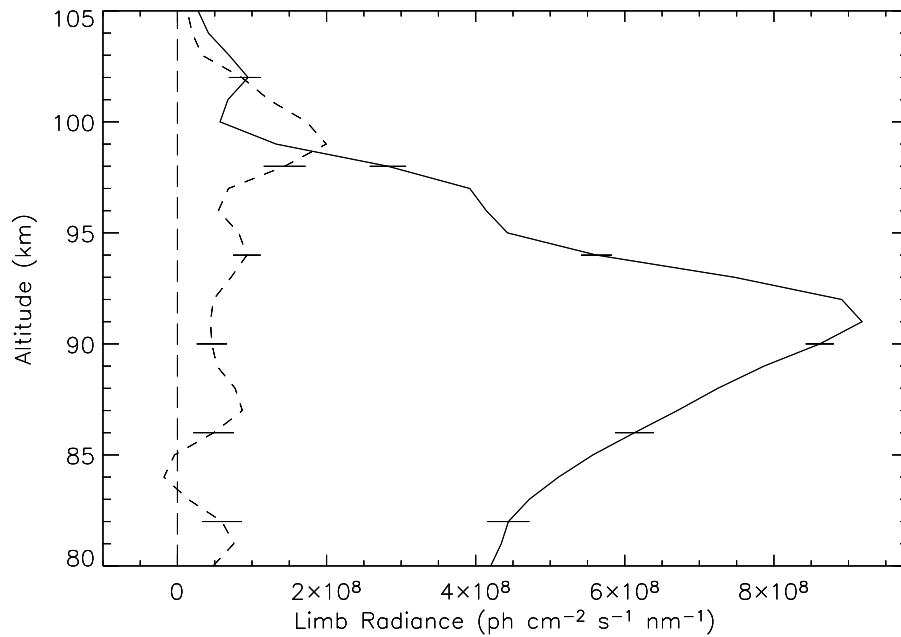


Figure 2. Limb radiance profiles of NO_2 continuum differential brightness at 580 nm, 9 May 2005, for the two cases in Figure 1. Solid, 75°S , 225°E ; dashed, 29°S , 221°E .

continuum measurement noise evaluated above; again, it is largely altitude independent.

[17] The Southern Hemisphere map shown in Figure 4 has been assembled from the approximately 130 NO_2 VER profiles obtained by OSIRIS over a 24 h period spanning 8–9 May 2005 for solar zenith angles greater than 101° . In this case, the units are again differential brightness at 580 nm; referred to the zenith, this simplifies comparisons with other observations of the NO_2 continuum emission, for example, zenith viewing ground-based instruments or rocket-borne

instruments (see below). The measurement noise, based on the measurement errors shown in Figure 3, is approximately 5×10^5 photons $\text{cm}^{-2} \text{s}^{-1} \text{nm}^{-1}$. Note that at midlatitudes and equatorial latitudes the zenith brightness values can include negative excursions when the observed signal levels approach the measurement noise. Also, as noted above, the subtracted OH night airglow includes a small NO_2 continuum component so that there is a systematic overcorrection of approximately 1×10^6 photons $\text{cm}^{-2} \text{s}^{-1} \text{nm}^{-1}$. Within the South Atlantic Anomaly, the noise level of the CCD detector

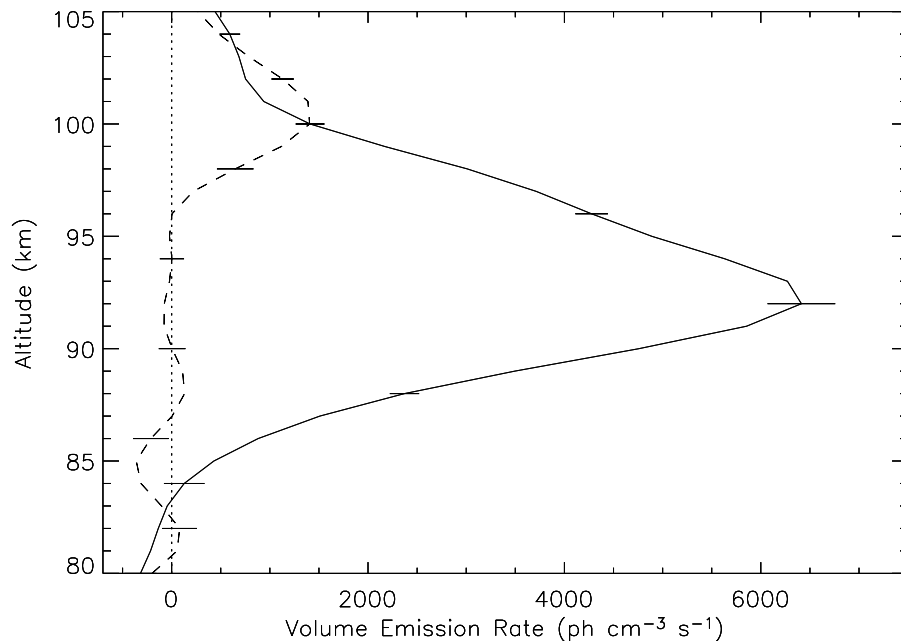


Figure 3. Volume emission rate profiles of total NO_2 continuum brightness, 9 May 2005, for the two limb scans referred to in Figure 1. Solid, 75°S , 225°E ; dashed, 29°S , 221°E .

Table 1. Estimates of Error Sources in the Analysis^a

Error Source	Systematic (%)	Reference	Measurement Noise
NO ₂ Continuum δ VER	15	Text	200 photons cm ⁻³ s ⁻¹
O ₂ (b ¹ Σ_g^+ - X ³ Σ_g^-) δ VER	10	Text	200 photons cm ⁻³ s ⁻¹
δ [O]	30	<i>Dickinson et al.</i> [1980]	
δT (°K) and δM (cm ⁻³)	10	MSIS and text	
OSIRIS RSS δ [O]	35	Text	2×10^{10} cm ⁻³
ACE-FTS RSS δ [O]	20	Text	1×10^{11} cm ⁻³
$\delta k_{(\text{NO}+\text{O})}$	15	<i>Becker et al.</i> [1972]	
$\delta k_{(\text{NO}+\text{O}+\text{M})}$	15	<i>Whytock et al.</i> [1976]	
OSIRIS RSS δ [NO]	30	Text	3×10^7 molecules cm ⁻³
ACE-FTS δ [NO]	10	<i>Kerzenmacher et al.</i> [2008]	2×10^7 molecules cm ⁻³

^aColumn 2 is the percentage systematic error of the measured signals. Column 4 is the instrument noise floor and is largely independent of altitude (text). RSS is the root sum squares of the individual error sources.

unfortunately increases above the typical NO₂ continuum signal level leading to anomalous results. With a measurement noise of approximately 5×10^5 photons cm⁻² s⁻¹ nm⁻¹, the signal-to-noise ratio for the brighter features shown in Figure 4 is near 20:1. Also included on Figure 4 are the maximum equatorward and poleward extents of the auroral oval over the 24 h observing period for active conditions [*Starkov, 1994*].

[18] It is instructive to compare the OSIRIS observations with other observations of the NO₂ continuum at auroral latitudes in the winter. The rocket-borne observations of *Witt et al.* [1981] and *Sharp* [1978] indicate a vertically

integrated differential brightness of approximately 1.6×10^7 photons cm⁻² s⁻¹ nm⁻¹ in the 520 nm region or approximately 1.8×10^7 photons cm⁻² s⁻¹ nm⁻¹ when referred to the continuum spectral peak at 580 nm. From Figure 4, the zenith brightness approaches 1.2×10^7 photons cm⁻² s⁻¹ nm⁻¹ at 580 nm, approximately 30% lower than the two rocket-borne observations. This could be considered qualitative agreement given the temporal change in the brightness of the NO₂ continuum as observed by OSIRIS in the dark polar region. For example, for the period 29–30 April 2005, the maximum zenith NO₂ continuum brightness observed by OSIRIS was approximately 0.3×10^7 photons cm⁻² s⁻¹ nm⁻¹

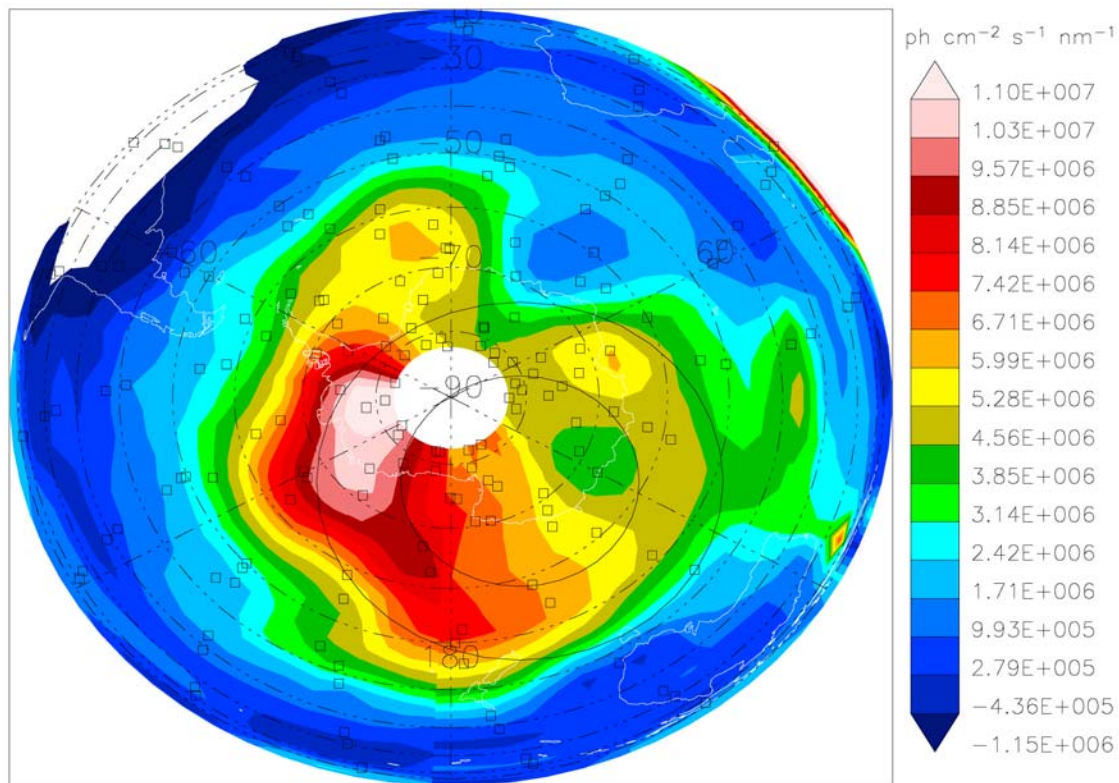


Figure 4. Southern Hemisphere map of NO₂ continuum differential brightness for 8–9 May 2005 as observed by OSIRIS. The units are referred to zenith observations at 580 nm. The squares mark the locations of OSIRIS limb profile measurements. Data in the South Atlantic Anomaly region are omitted due to excessive detector noise. The concentric circles (solid) offset from the geographic pole indicate the auroral oval maximum equatorward and poleward extents over the 24 h period for active conditions.

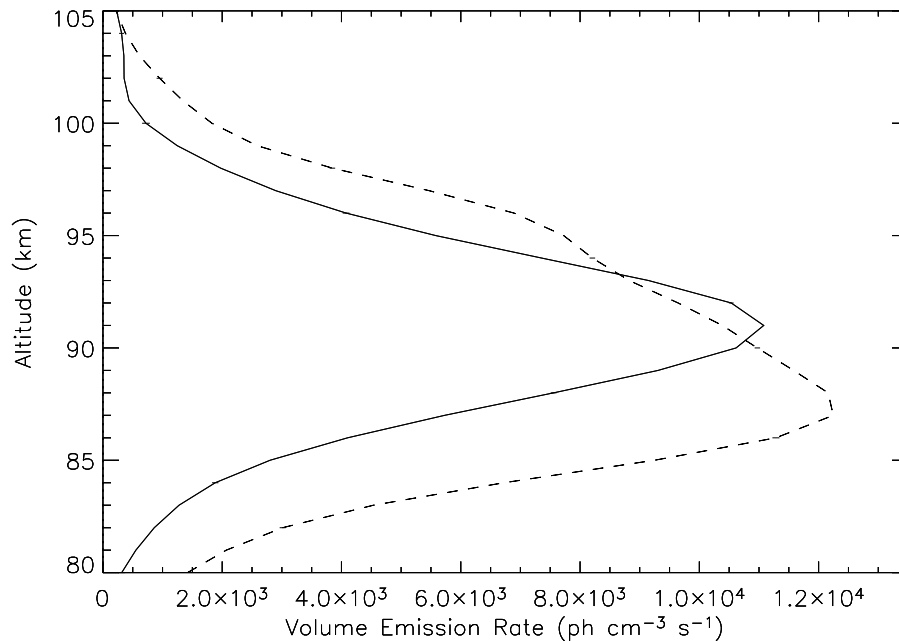


Figure 5. Volume emission rate profiles of the 762 nm $O_2(b^1\Sigma_g^+ - X^3\Sigma_g^-)$ 0-0 band, 9 May 2005, for the two limb scans referred to in Figure 1. Solid, 75°S, 225°E; dashed, 29°S, 221°E.

whereas for 17–18 May 2005 the maximum was approximately 1.7×10^7 photons $cm^{-2} s^{-1} nm^{-1}$.

[19] Systematic error sources not included in the above discussion of the NO_2 continuum include a 10% OSIRIS absolute calibration uncertainty plus an estimated uncertainty of 10% in the spectral shape of the NO_2 continuum emission profile. Combined quadratically, the systematic uncertainty approaches 15% (Table 1). The systematic error is a percentage of the derived signal and is thus altitude dependent, in contrast to the measurement error described above, which is largely altitude independent.

3. Deriving Atomic Oxygen Densities From OSIRIS and ACE-FTS Observations

[20] As indicated previously, [O] is required to infer [NO] from the NO_2 continuum observations through the reaction $NO + O(+M) \rightarrow NO_2^*(+M)$. The first [O] analysis described here relies on a derived product based on the $O + O + M \rightarrow O_2(b^1\Sigma_g^+) + M$ reaction and the 762 nm $O_2(b^1\Sigma_g^+ - X^3\Sigma_g^-)$ 0-0 band emission profile measured by OSIRIS. *McDade et al.* [1986b] have derived conversion coefficients that relate measured 762 nm VER to measured [O], and *Alfaro Suzán* [2009] has subsequently derived an analytic solution for the second order coefficients. Using simulations *Gumbel and Witt* [1997] have extended the analysis techniques. The derived [O] values shown below are averages of the two limiting cases for the MSIS-83 solutions of *McDade et al.* [1986b]. The temperature and density profiles are from the updated MSIS model [*Picone et al.*, 2002].

[21] Examples of the $O_2(b^1\Sigma_g^+ - X^3\Sigma_g^-)$ 0-0 band VER altitude profiles, calculated from OSIRIS limb radiance profiles, are shown in Figure 5. The 0-0 band emission is typically the brightest feature in the OSIRIS night airglow spectrum leading to an excellent signal-to-noise ratio in the

derived VER profiles, the measurement uncertainty is approximately 200 photons $cm^{-3} s^{-1}$ (Table 1). As discussed above, these VER profiles are used to derive the [O] profiles shown in Figure 6, which are required for the derivation of [NO] from the NO_2 continuum observations.

[22] For comparison with [O] profiles derived from OSIRIS observations, an [O] profile obtained from WINDII observations [*Russell et al.*, 2005] for fall, 30°N is also included in Figure 6. WINDII results cover only equatorial to midlatitudes. Above 92 km the OSIRIS [O] profile at 29°S and 221°E is within 20% of the WINDII profile, while at lower altitudes OSIRIS [O] is considerably larger. To demonstrate the longitudinal variability of [O] as observed by OSIRIS a third [O] curve derived from the $O_2(b^1\Sigma_g^+ - X^3\Sigma_g^-)$ 0-0 band is included, again at 29°S but displaced to 293°E, approximately 19 LST. In this case the derived [O] is approximately 40% lower than observed at 29°S and 221°E. This longitudinal and latitudinal variability of [O], discussed again below, is a common feature of the OSIRIS observations for the 8–9 May 2005 period. Also included in Figure 6 is the MSIS [O] profile [*Picone et al.*, 2002], 30°S, 9 May 2005. The two OSIRIS [O] profiles at 29°S bracket the MSIS profile above 90 km but are larger at lower altitudes. The WINDII profile is within 15% of the MSIS profile.

[23] A map of the Southern Hemisphere [O] values derived from the OSIRIS $O_2(b^1\Sigma_g^+ - X^3\Sigma_g^-)$ observations is shown in Figure 7 for a fixed altitude of 90 km. Because the OSIRIS $O_2(b^1\Sigma_g^+ - X^3\Sigma_g^-)$ 0-0 band signal is much stronger than the OSIRIS NO_2 continuum signal, the increased detector noise in the South Atlantic Anomaly does not have a serious impact on the measured 0-0 band. Since auroral contamination of the $O_2(b^1\Sigma_g^+ - X^3\Sigma_g^-)$ 0-0 band in the 80–100 km range will produce erroneous [O] profiles, those profiles for which aurora is detected, through the 558 nm emission brightness, are rejected. It is readily apparent from

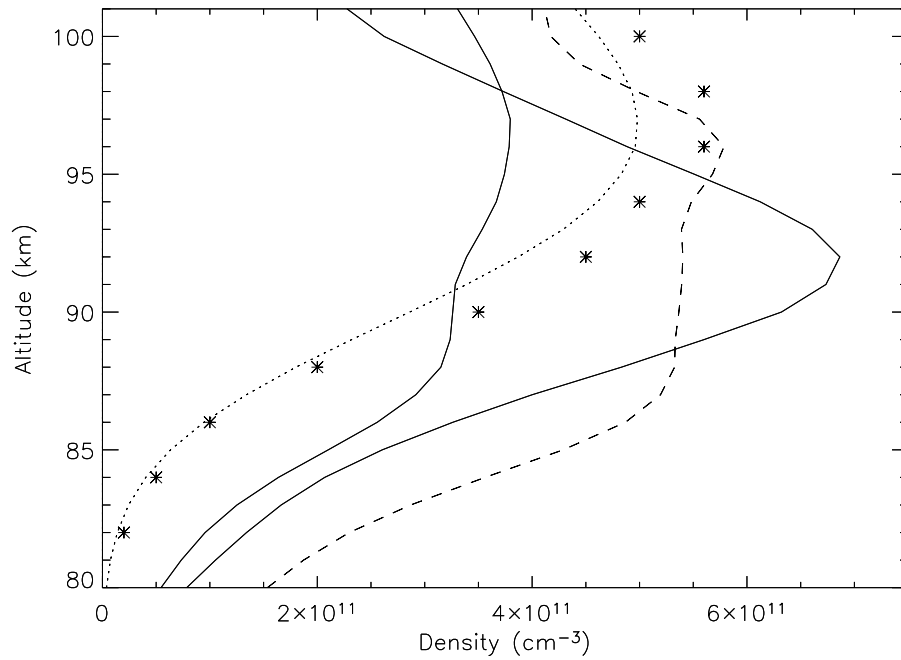


Figure 6. Atomic oxygen density profiles derived from the $O_2(b^1\Sigma_g^+ - X^3\Sigma_g^-)$ 0-0 band VER profiles in Figure 5, 9 May 2005, for the two limb scans referred to in Figure 1. Solid, 75°S, 225°E; dashed, 29°S, 221°E. The measurement uncertainty is approximately $2 \times 10^{10} \text{ cm}^{-3}$ over the altitude range. Also included for comparison: dot-dot-dash, OSIRIS 29°S, 293°E; dot, MSIS 30°S, 9 May 2005; asterisk, WINDII 30°N, fall.

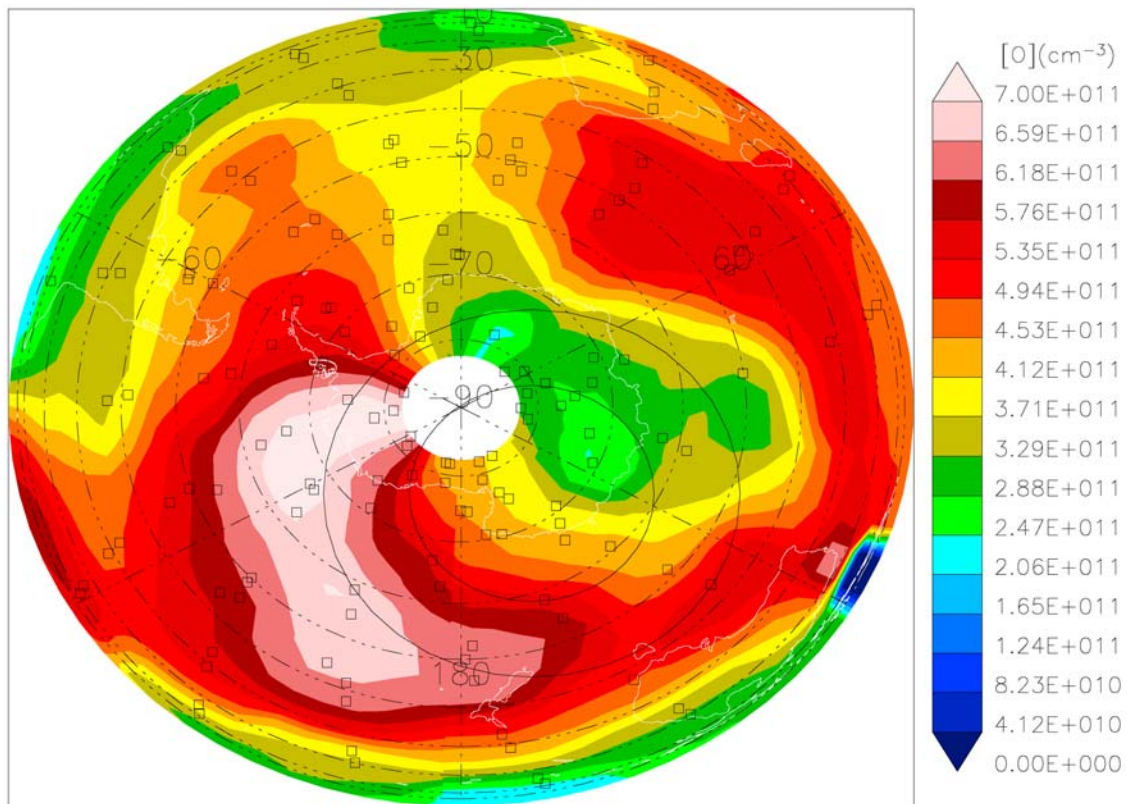


Figure 7. Southern Hemisphere polar projection of atomic oxygen density at 90 km altitude, for 8–9 May 2005, derived from OSIRIS $O_2(b^1\Sigma_g^+ - X^3\Sigma_g^-)$ 0-0 band observations. The extents of the auroral oval are shown as in Figure 4.

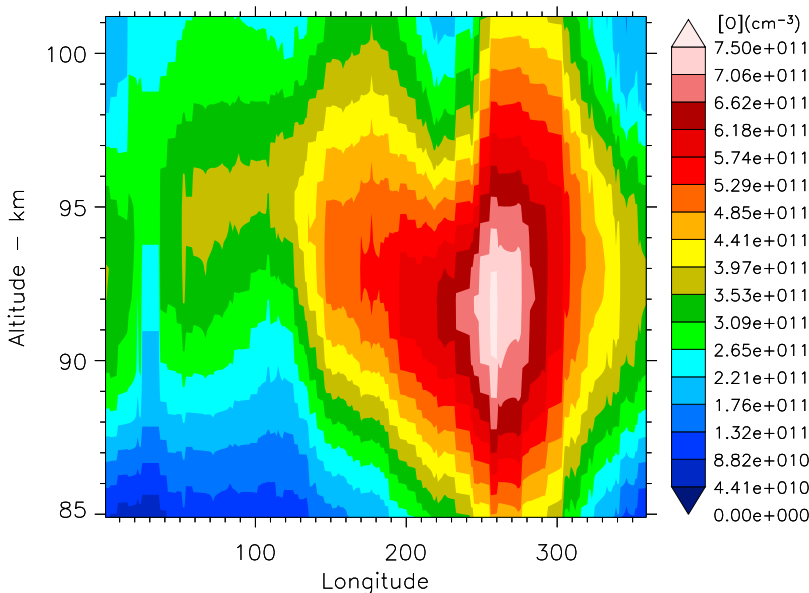


Figure 8. Atomic oxygen density profile versus longitude derived from OSIRIS $O_2(b^1\Sigma_g^+ - X^3\Sigma_g^-)$ 0–0 band observations, 8–9 May 2005, for profiles between 70°S and 80°S.

Figure 7 that the [O] spatial distribution at 90 km is highly variable.

[24] To demonstrate this [O] variability further, a plot of the [O] vertical distribution as a function of longitude within a 10° latitude range centered on 75°S is shown in Figure 8. The derived densities vary by at least a factor of two with longitude over the 85–100 km altitude range, precisely the range of the observed NO_2 continuum emission. By way of comparison, for an assumed uncertainty of 10% in MSIS temperature and density (Table 1), model simulations indicate derived [O] values based on the coefficients provided by *McDade et al.* [1986b] vary by approximately 20%, much less than the factor of two seen in Figure 8. For a reliable derivation of [NO] based on the $NO + O(+M) \rightarrow NO_2^*(+M)$ reaction, it is apparent that the spatial variability of [O] must be included in the analysis described below. The OSIRIS observations of the NO_2 continuum and of [O] are from common volumes.

[25] A 10% systematic uncertainty in the OSIRIS absolute calibration for the $O_2(b^1\Sigma_g^+ - X^3\Sigma_g^-)$ 0–0 band (Table 1) is not included in the above analysis. Also, *Dickinson et al.* [1980] have estimated a systematic error of up to 30% for their [O] measurement technique (Table 1). Uncertainties in the background atmosphere temperature and density, discussed above, also contribute to the derived [O] error. Combining these uncertainties leads to a root sum squares systematic error of approximately 35% (Table 1) for the OSIRIS [O] determination. This error will contribute an equivalent percentage error component to the derived OSIRIS [NO] values discussed in the following sections. In an effort to reduce this large uncertainty, independent [O] measurement approaches were investigated.

[26] *Smith and Marsh* [2005] describe a technique for deriving [O] from daytime $[O_3]$ measurements based on the equilibrium between O_3 loss by photodissociation and O_3 production via the $O + O_2 + M \rightarrow O_3 + M$ reaction. Thus, ACE-FTS $[O_3]$ measurements over the 85–90 km range can

potentially be used to infer [O]. On the basis of model calculations [*e.g.*, *Smith and Marsh*, 2005], the lifetime of O near 88 km, the altitude chosen here for comparison with the derived [O] from OSIRIS 762 nm observations, is considerably longer than the approximately 5 h time difference between the ACE-FTS sunset measurements and the OSIRIS ascending node night measurements. Briefly, the ACE-FTS instrument measures terrestrial limb solar infrared absorption spectra from 750 to 4400 cm^{-1} during sunrise and sunset to obtain vertical profiles of numerous atmospheric species. The vertical sampling interval ranges from 2 to 6 km with a vertical field of view of 3 km. Absolute limb-pointing knowledge is better than one-half kilometer; details of the analysis and profile generation have been given by *Boone et al.* [2005]. Very significantly, the ACE-FTS version 2.2 data set also includes measured temperature [*Sica et al.*, 2008] and atmospheric density profiles for each occultation. *Dupuy et al.* [2009] describe the validation of the ACE-FTS ozone measurements but only below 65 km. Atomic oxygen densities along a longitude circle derived from ACE-FTS $[O_3]$ sunset observations on 8–9 May 2005 at 67°S and approximately 15 LST are shown in Figure 9. The ACE-FTS measurement uncertainty in $[O_3]$ at 88 km is approximately 1×10^8 molecules cm^{-3} , which equates to an uncertainty in [O] of approximately 1×10^{11} molecules cm^{-3} . The systematic uncertainty in the determination of [O] from ACE-FTS $[O_3]$ is estimated to be approximately 20%, the major error components being the measured ACE-FTS background density and temperature and the three-body reaction rate [*Sander et al.*, 2006].

[27] The longitudinal variation of [O] derived from OSIRIS 762 nm observations is also included in Figure 9, both for ascending node at approximately 20 LST and descending node at approximately 05 LST. In this case, the latitude range included in the OSIRIS analysis is from 62°S to 72°S, that is, within 5° of latitude of the ACE-FTS occultations. Also, the ACE-FTS measured temperature and density

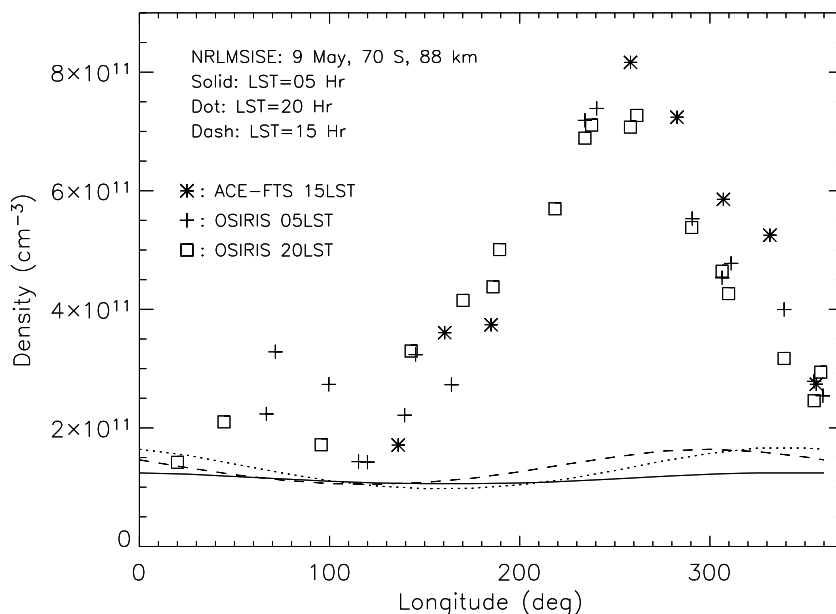


Figure 9. [O] versus longitude derived from ACE-FTS sunset [O₃] observations at 88 km, 67°S, compared with [O] derived from OSIRIS O₂ 762 nm observations at 88 km, 62°S–72°S, both for 8–9 May 2005. NRLMSISE-00 profiles for [O] are also shown for 9 May at 88 km for the corresponding local solar times (LST).

profiles are assumed for the OSIRIS calculations in order to be consistent with the ACE-FTS analysis. From Figure 9 the OSIRIS derived [O] values would have to be scaled upward by approximately 15% to match the maximum ACE-FTS derived [O] values. This 15% uncertainty is well within the combined error range for the two observations, 35% for OSIRIS [O] and 20% for ACE-FTS [O] (Table 1). In the NO analyses described below the OSIRIS derived [O] is arbitrarily scaled upward by 5% to approach the ACE-FTS derived [O] values. It is estimated that the systematic error of the combined [O] results is approximately 20%. It should be noted that the derived [O] from each of the two observational data sets is considerably in excess of the model NRLMSISE-00 [O] values; this is also included in Figure 9 for the matching LST. Averaged over longitude the derived [O] is approximately $4 \times 10^{11} \text{ cm}^{-3}$.

4. Deriving NO Densities From the OSIRIS NO₂ and O Observations

[28] Deriving [NO] from $\text{NO} + \text{O}(+M) \rightarrow \text{NO}_2^*(+M)$ requires values for reaction rates, atmospheric temperature (T), and density ($[M]$), [O] and NO₂ VER. The bimolecular reaction rate $k_{(\text{NO} + \text{O})}$ is $4.2 \times 10^{-18} \text{ cm}^3 \text{ molecule}^{-1} \text{ s}^{-1}$ [Becker *et al.*, 1972] and the termolecular rate $k_{(\text{NO} + \text{O} + M)}$ is $15.5 \times 10^{-33} \exp(1160/1.987T) \text{ cm}^6 \text{ molecule}^{-2} \text{ s}^{-1}$ [Whytock *et al.*, 1976]. Rate error estimates are given in Table 1. Again, the temperature and density profiles are from the updated MSIS model [Picone *et al.*, 2002]. The procedures used for obtaining NO₂ VER and [O] have been discussed in the previous two sections.

[29] The derived NO profiles shown in Figure 10 are obtained using the measured OSIRIS NO₂ VER profiles shown in Figure 3, and the derived [O] profiles shown in

Figure 6 are scaled upward by 5% as noted previously. The profile at 75°S shows [NO] values that are considerably larger than those at 29°S; this follows from the two NO₂ VER profiles shown in Figure 3. The profile obtained at 29°S shows very little NO below 95 km but measurable amounts in the 100 km region; this is perhaps not unexpected when compared with [NO] values at 30° latitude and 106 km altitude reported by Barth *et al.* [2003] in their Figure 10 when auroral activity is occurring at polar latitudes. The OSIRIS NO₂ VER and [O] measurement errors lead to a derived [NO] noise-limited detection threshold of approximately $3 \times 10^7 \text{ cm}^{-3}$ and an estimated systematic error of 30% in the 85–100 km range. As discussed above, the derived [NO] values are systematically too low by approximately $5 \times 10^7 \text{ cm}^{-3}$ due to the inclusion of a small amount of NO₂ continuum in the OH night airglow subtraction spectrum.

[30] A map of the Southern Hemisphere [NO] values derived from the OSIRIS observations and averaged over the 88–92 km altitude range is shown in Figure 11. As expected, the increased NO densities occur in the predominantly dark polar region. Additionally, there is considerable longitudinal variability in the [NO] geographic distribution. As in Figure 4, the maximum equatorward and poleward extents of the auroral oval for active conditions are indicated.

[31] Similar to the [O] profile above (Figure 8), a plot of the OSIRIS [NO] vertical distribution as a function of longitude within a 10° latitude range centered on 75°S is shown in Figure 12. At any given altitude, the derived [NO] varies by a factor of two or more with longitude. The NO density increases with increasing altitude at most longitudes. For an assumed uncertainty of 10% in MSIS temperature and density (Table 1), model simulations, including the offsetting effect on derived [O], indicate [NO] values vary by

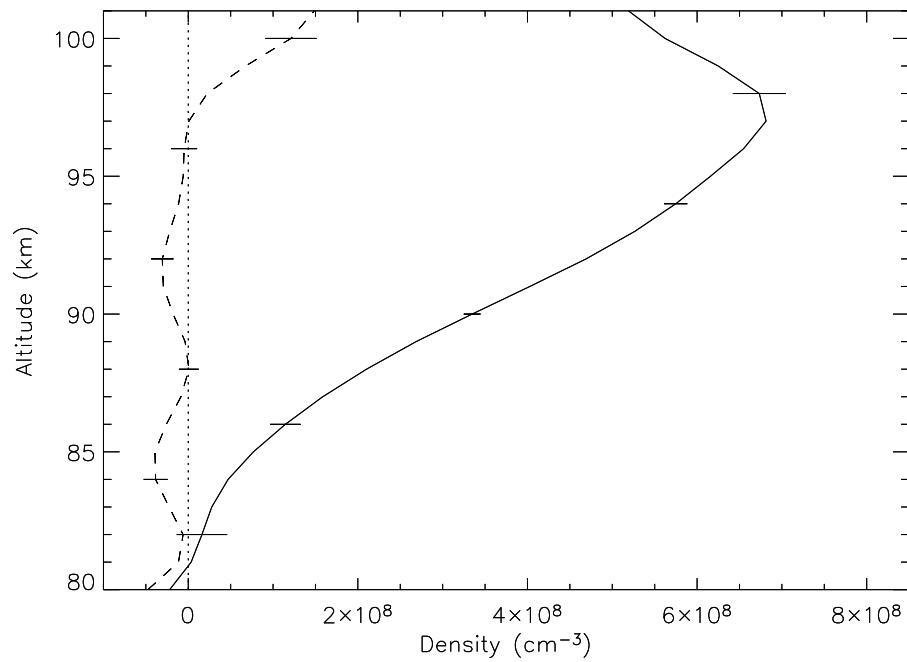


Figure 10. NO density profiles for 9 May 2005, for the two limb scans referred to in Figure 1. Solid, 75°S, 225°E; Dashed, 29°S, 221°E. The profiles are derived using the NO₂ VER profiles in Figure 3, and the [O] profiles in Figure 6 scaled upward by 5% (see text).

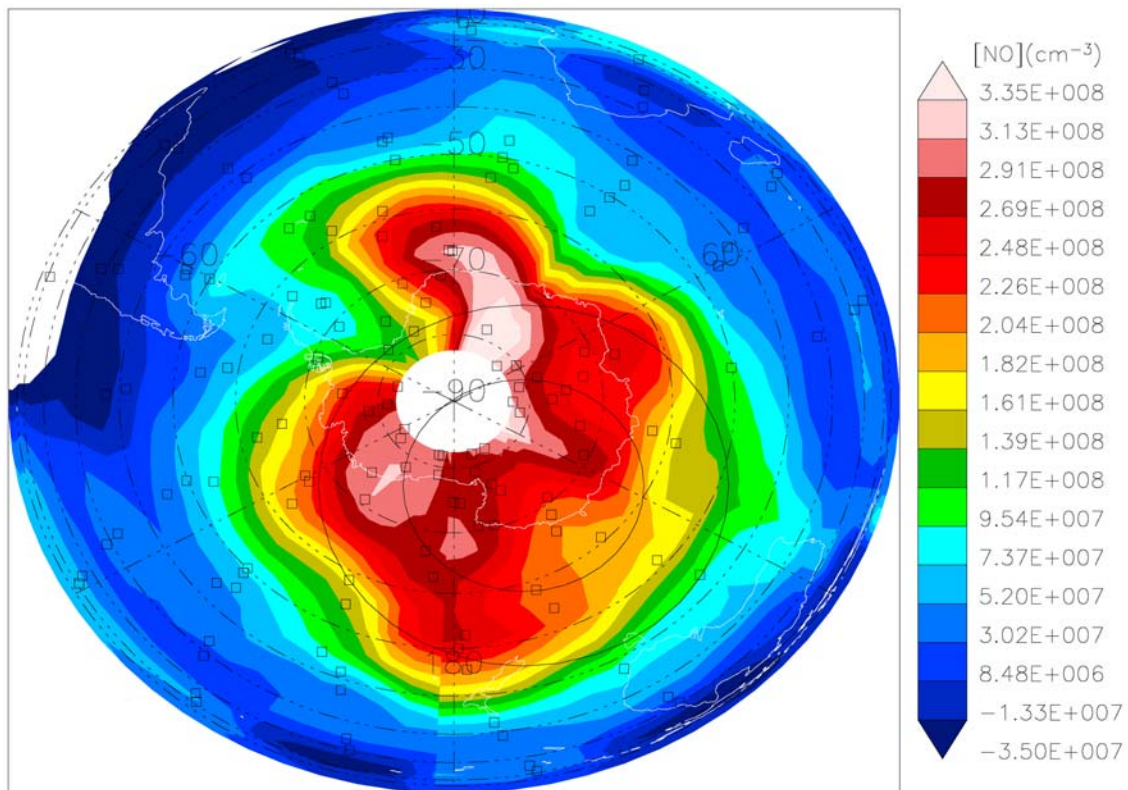


Figure 11. Southern Hemisphere polar projection of the NO density derived from OSIRIS observations, 8–9 May 2005, averaged over the 88–92 km altitude range. The equatorial and polar extents of the auroral oval are shown as in Figure 4.

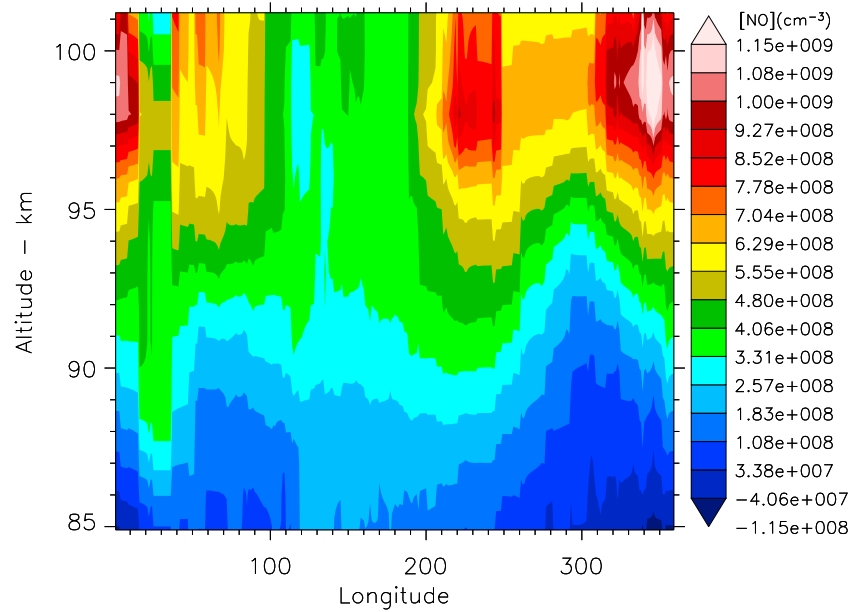


Figure 12. Derived NO density vertical profile versus longitude for OSIRIS observations, 8–9 May 2005, for profiles between 70°S and 80°S.

approximately 10%, much less than the factor of two seen in Figure 12.

5. Comparison of OSIRIS Derived [NO] With ACE-FTS Measured [NO]

[32] The ACE-FTS NO measurements are described in detail by Kerzenmacher *et al.* [2008] and the error estimates are listed in Table 1. The validity of the comparison between the ACE-FTS NO sunset observations and the OSIRIS

derived NO night observations approximately 5 h later stems from the long photochemical lifetime of NO under the observing conditions. From model simulations, it is estimated that the [NO] lifetime is approximately 10 days for early May conditions at 65°S. However, for correlative observations separated by tens of hours the horizontal winds can potentially affect the accuracy of the comparisons. A comparison is shown in Figure 13 between observed ACE-FTS [NO] and derived OSIRIS [NO]. The [NO] values are averaged over the 85–95 km region. Atmospheric density

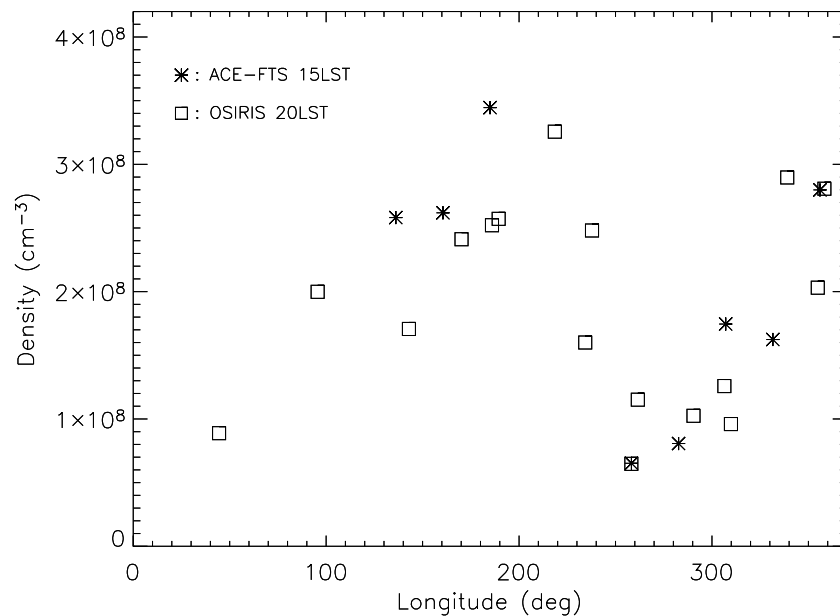


Figure 13. Comparing ACE-FTS NO measured density (averaged over 85–95 km altitude range, occultations at 67°S, approximately 15 LST) with OSIRIS-derived NO density (average over 85–95 km altitude range, including profiles between 62°S and 72°S, ascending node at approximately 20 LST). All data are from 8 to 9 May 2005.

and temperature profiles are taken from the ACE-FTS data base. Again, as discussed previously, the OSIRIS derived [O] values are scaled upward by 5%. From Table 1 the root sum squares (RSS) systematic error for the OSIRIS determination of [NO] is 30%. Given the significant spatial gradients in the [NO] distribution derived from the OSIRIS observations (Figures 11 and 12), the scatter evident in Figure 13 can be expected.

6. Discussion

[33] The $\text{NO} + \text{O}(+M) \rightarrow \text{NO}_2^*(+M) + h\nu$ reaction produces a chemiluminescent continuum spectrum that is detected in the predominantly dark upper mesospheric polar regions by the OSIRIS spectrograph on the Odin spacecraft. After removal of the OH night airglow component, NO_2 limb radiance profiles are calculated for individual OSIRIS limb scans. Volume emission rate altitude profiles of the NO_2 continuum are computed from the limb radiance profiles over the 80–100 km range. The sample NO_2 continuum Southern Hemisphere map, shown here for 8–9 May 2005, exhibits considerable spatial variability in both latitude and longitude.

[34] Through another series of calculations the altitude profiles of [O] are derived from OSIRIS $\text{O}_2(\text{b}^1\Sigma_g^+ - \text{X}^3\Sigma_g^-)$ 0–0 band observations. These derived [O] results are compared with [O] values determined from ACE-FTS sunset $[\text{O}_3]$ measurements. For the derivation of [NO] from the NO_2 chemiluminescent continuum, the [O] values intermediate between the two methods are assumed. Significant spatial variability in both latitude and longitude is observed in measured [O] for early May in the Southern Hemisphere. Specifically, there is a pronounced [O] minimum located between 60°S and 80°S at approximately 60° east along with an [O] maximum displaced in longitude by approximately 180°. These paired minimum and maximum features at approximately 70°S are frequently present in the OSIRIS derived [O] from May through August 2005. From Figure 9, the major [O] features appear to be independent of local time. No explanation is offered for this observed variability in [O] geographic distribution. NRLMSISE [Picone *et al.*, 2002] model distributions of [O] at 88 km, 70°S, are considerably smaller than those derived from both the OSIRIS 762 nm night and the ACE-FTS $[\text{O}_3]$ sunset observations.

[35] The [NO] derived from the OSIRIS NO_2 continuum and the [O] observations is shown in Figure 11. The [NO] measurement uncertainty over the 85–95 km altitude range is approximately 3×10^7 molecules cm^{-3} . The [NO] map shows marked differences in geographic distribution from the [O] map in Figure 7. Comparison between OSIRIS derived [NO] and ACE-FTS solar occultation observation of [NO] shows qualitative agreement. This comparison, which includes a very limited number of measurements, does not constitute a validation of the OSIRIS [NO] measurements. A future study will deal with the comparisons more extensively.

[36] The spatial distribution of derived [NO] in Figure 11 shows a pronounced longitudinal asymmetry and an extension toward midlatitudes into a region with increasing sunlit hours. It is instructive to compare this very structured NO spatial distribution with the auroral precipitation patterns occurring just before and during the OSIRIS 8–9 May 2005 observations. The period begins on 8 May 2005, 13 UT,

near the peak of an intense geomagnetic storm, Ap 236 (<ftp://ftp.ngdc.noaa.gov>). Particle flux measurements (<http://poes.ngdc.noaa.gov>) over the same time period indicate the presence of electrons with energies greater than 30 keV, sufficient to penetrate below 100 km; this is not typical but is often present as evidenced by type b auroral events [Vallance Jones, 1974]. Accordingly, a portion of the OSIRIS derived NO below 100 km was likely produced below 100 km. From an initial inspection of the TIMED Global Ultraviolet Imager (GUVI) LBH1 orbit images [Christensen *et al.*, 2003], the composite southern polar auroral excitation pattern observed on 8 May 2005 in the auroral oval is qualitatively very similar to the OSIRIS-derived NO spatial distribution shown in Figure 11. In particular, the extension of OSIRIS-derived NO to approximately 50°S, 180°E–240°E, closely matches the GUVI precipitation pattern. This apparent correlation requires a quantitative analysis to assess the similarity in spatial distribution between OSIRIS derived [NO] and GUVI LBH1 images. Also from Figure 11, in the dark region nearest the pole, a portion of the NO observed below 100 km is possibly due to normal auroral activity over the previous weeks, assuming polar atmospheric descent rates of a few hundred meters per day [Funke *et al.*, 2005]. Also, horizontal winds with drift rates of approximately 1000 km d^{-1} in the 95 km altitude southern polar region [Drob *et al.*, 2008] will have an impact on the observed NO spatial distribution.

[37] OSIRIS derived [NO] values from 80 to 100 km are available over most of the Southern Hemisphere for periods from May through August from 2003 to 2009. Due to the Odin orbit inclination, the useful observing period in the Northern Hemisphere is limited to approximately 1 month around winter solstice. This capability of tracking [NO] in the MLT when the polar regions are predominantly in darkness complements independent daytime observations of thermospheric [NO] to provide near-continuous temporal coverage in the auroral region.

[38] **Acknowledgments.** This work was supported by the Canadian Space Agency and the Natural Sciences and Engineering Research Council (Canada). Odin is a Swedish-led satellite project funded jointly by Sweden (SNSB), Canada (CSA), France (CNES), and Finland (Tekes). ACE is supplied by the CSA. Support was also provided by the U.K. Natural Environment Research Council (NERC). Auroral oval corrected geomagnetic coordinate transformations were obtained from PDF/Modelweb. The authors gratefully acknowledge the constructive suggestions provided by the reviewers for improving the manuscript.

References

- Alfaro Suzán, A. L. (2009), Airglow studies using observations made with the GLO instrument on the Space Shuttle, Ph.D. Dissertation, York University, Toronto, Canada.
- Bailey, S. M., C. A. Barth, and S. C. Solomon (2002), A model of nitric oxide in the lower thermosphere, *J. Geophys. Res.*, *107*(A8), 1205, doi:10.1029/2001JA000258.
- Barth, C. A., K. D. Mankoff, S. M. Bailey, and S. C. Solomon (2003), Global observations of nitric oxide in the thermosphere, *J. Geophys. Res.*, *108*(A1), 1027, doi:10.1029/2002JA009458.
- Becker, K. H., W. Groth, and D. Thran (1972), The mechanism of the air-afterglow $\text{NO} + \text{O} \rightarrow \text{NO}_2 + h\nu$, *Chem. Phys. Lett.*, *15*, 215–220.
- Bernath, P. F., et al. (2005), Atmospheric Chemistry Experiment (ACE): Mission overview, *Geophys. Res. Lett.*, *32*, L15S01, doi:10.1029/2005GL022386.
- Boone, C. D., R. Nassar, K. A. Walker, Y. Rochon, S. D. McLeod, C. P. Rinsland, and P. F. Bernath (2005), Retrievals for the atmospheric chem-

- istry experiment Fourier transform spectrometer, *Appl. Optics*, *44*, 7218–7231.
- Bourassa, A. E., D. A. Degenstein, and E. J. Llewellyn (2008), SASK-TRAN: A spherical geometry radiative transfer code for efficient estimation of limb scattered sunlight, *J. Quant. Spectrosc. Radiat. Transfer*, *109*, 52–73, doi:10.1016/j.jqsrt.2007.07.007.
- Broadfoot, A. L., and K. R. Kendall (1968), The airglow spectrum, 3100–10,100 Å, *J. Geophys. Res.*, *73*, 426–428.
- Christensen, A. B., et al. (2003), Initial observations with the Global Ultraviolet Imager (GUVI) in the NASA TIMED satellite mission, *J. Geophys. Res.*, *108*(A12), 1451, doi:10.1029/2003JA009918 (guvi.jhuapl.edu).
- Dickinson, P. H. G., W. C. Bain, L. Thomas, E. R. Williams, D. B. Jenkins, and N. D. Twiddy (1980), The Determination of the atomic oxygen concentration and associated parameters in the lower ionosphere, *Proc. R. Soc. London, Ser. A*, *369*, 379–408.
- Drob, D. P., et al. (2008), An empirical model of the Earth's horizontal wind fields: HWM07, *J. Geophys. Res.*, *113*, A12304, doi:10.1029/2008JA013668.
- Dupuy, E., et al. (2009), Validation of ozone measurements from the Atmospheric Chemistry Experiment (ACE), *Atmos. Chem. Phys.*, *9*, 287–343.
- Funke, B., M. López-Puertas, S. Gil-López, T. von Clarmann, G. P. Stiller, H. Fischer, and S. Kellmann (2005), Downward transport of upper atmospheric NO_x into the polar stratosphere and lower mesosphere during the Antarctic 2003 and Arctic 2002/2003 winters, *J. Geophys. Res.*, *110*, D24308, doi:10.1029/2005JD006463.
- Gattinger, R. L., D. A. Degenstein, and E. J. Llewellyn (2006), Optical Spectrograph and Infra-Red Imaging System (OSIRIS) observations of mesospheric OH A²Σ⁺ – X²Π 0-0 and 1-1 band resonance emissions, *J. Geophys. Res.*, *111*, D13303, doi:10.1029/2005JD006369.
- Gattinger, R. L., W. F. J. Evans, I. C. McDade, D. A. Degenstein, and E. J. Llewellyn (2009), Observation of the chemiluminescent NO + O → NO₂ + hν reaction in the upper mesospheric dark polar regions by OSIRIS on Odin, *Can. J. Phys.*, *87*, 925–932, doi:10.1139/P09-051.
- Gumbel, J., and G. Witt (1997), Monte Carlo studies of the resonance fluorescence technique for atmospheric atomic oxygen measurements, *J. Quant. Spectrosc. Radiat. Transfer*, *58*, 1–17.
- Hauchecorne, A., J.-L. Bertaux, F. Dalaudier, J. M. Russell III, M. G. Mlynczak, E. Kyrola, and D. Fussen (2007), Large increase of NO₂ in the north polar mesosphere in January–February 2004: Evidence of a dynamical origin from GOMOS/ENVISAT and SABER/TIMED data, *Geophys. Res. Lett.*, *34*, L03810, doi:10.1029/2006GL027628.
- Jucks, K. W., D. G. Johnson, K. V. Chance, W. A. Traub, R. J. Salawitch, and R. A. Stachnik (1996), Ozone production and loss rate measurements in the middle stratosphere, *J. Geophys. Res.*, *101*(D22), 28,785–28,792.
- Kerzenmacher, T., et al. (2008), Validation of NO₂ and NO from the Atmospheric Chemistry Experiment (ACE), *Atmos. Chem. Phys.*, *8*, 5801–5841.
- Llewellyn, E. J., et al. (2004), The OSIRIS instrument on the Odin spacecraft, *Can. J. Phys.*, *82*, 411–422.
- McDade, I. C., E. J. Llewellyn, R. G. H. Greer, and D. P. Murtagh (1986a), ETON 3: Altitude profiles of the nightglow continuum at green and near infrared wavelengths, *Planet. Space Sci.*, *34*, 801–810.
- McDade, I. C., D. P. Murtagh, R. G. H. Greer, P. H. G. Dickinson, G. Witt, J. Stegman, E. J. Llewellyn, L. Thomas, and D. B. Jenkins (1986b), ETON 2: Quenching parameters for the proposed precursors of O₂(b¹Σ_g⁺) and O(¹S) in the terrestrial nightglow, *Planet. Space Sci.*, *34*, 789–800.
- Murtagh, D., et al. (2002), An overview of the Odin atmospheric mission, *Can. J. Phys.*, *80*, 309–319.
- Picone, J. M., A. E. Hedin, D. P. Drob, and A. C. Aikin (2002), NRL-MSISE-00 empirical model of the atmosphere: Statistical comparisons and scientific issues, *J. Geophys. Res.*, *107*(A12), 1468, doi:10.1029/2002JA009430.
- Randall, C. E., V. I. Harvey, C. S. Singleton, P. F. Bernath, C. D. Boone, and J. U. Kozyra (2006), Enhanced NO_x in 2006 linked to strong upper stratospheric Arctic vortex, *Geophys. Res. Lett.*, *33*, L18811, doi:10.1029/2006GL027160.
- Russell, J. M., III, S. Solomon, L. Gordley, E. Remsburg, and L. Callis (1984), The variability of stratospheric and mesospheric NO₂ in the polar winter night observed by LIMS, *J. Geophys. Res.*, *89*(D5), 7267–7275.
- Russell, J. P., W. E. Ward, R. P. Lowe, R. G. Roble, G. G. Shepherd, and B. H. Solheim (2005), Atomic oxygen profiles (80–115 km) derived from WINDII/UARS measurements of the hydroxyl and greenline airglow: II. Local time-latitude dependence, *J. Geophys. Res.*, *110*, D15305, doi:10.1029/2004JD005570.
- Sander, S. P., et al. (2006), Chemical kinetics and photochemical data for use in atmospheric studies, Jet Propulsion Laboratory Publications 06-02, Evaluation Number 15, 10 July.
- Sharp, W. E. (1978), NO₂ continuum in aurora, *J. Geophys. Res.*, *83*, 4373–4376.
- Sica, R. J., et al. (2008), Validation of the Atmospheric Chemistry Experiment (ACE) version 2.2 temperature using ground-based and spaceborne measurements, *Atmos. Chem. Phys.*, *8*, 35–62.
- Siskind, D. E., G. E. Nedoluha, C. E. Randall, M. Fromm, and J. M. Russell III (2000), An assessment of Southern Hemisphere stratospheric NO_x enhancements due to transport from the upper atmosphere, *Geophys. Res. Lett.*, *27*, 329–332.
- Smith, A. K., and D. R. Marsh (2005), Processes that account for the ozone maximum at the mesopause, *J. Geophys. Res.*, *110*, D23305, doi:10.1029/2005JD006298.
- Solomon, S., P. J. Crutzen, and R. G. Roble (1982), Photochemical coupling of the thermosphere and the lower atmosphere: 1. Odd nitrogen from 50 to 120 km, *J. Geophys. Res.*, *87*, 7206–7220.
- Starkov, G. V. (1994), Mathematical model of the auroral boundaries, *Geomagn. Aeron., Engl. Trans.*, *34*, 331–336.
- Stewart, D. T. (1957), A spectrophotometric observation of the air afterglow, *J. Atmos. Terr. Phys.*, *10*, 318–319.
- Vallance Jones, A. (1974), *Aurora*, D. Reidel, Dordrecht, Holland.
- Vogel, B., P. Konopka, J.-U. GroöB, R. Müller, B. Funke, M. Lopez-Puertas, T. Reddmann, G. Stiller, T. von Clarmann, and M. Riese (2008), Model simulations of stratospheric ozone loss caused by enhanced mesospheric NO_x during Arctic Winter 2003/2004, *Atmos. Chem. Phys.*, *8*, 5279–5293.
- von Savigny, C. H., I. C. McDade, G. G. Shepherd, and Y. Rochon (1999), Lower thermospheric nitric oxide concentrations derived from WINDII observations of the green nightglow continuum at 553 nm, *Ann. Geophys.*, *17*, 1439–1446.
- Whytock, D. A., J. V. Michael, and W. A. Payne (1976), Absolute rate constants for O + NO + N₂ → NO₂ + N₂ from 217–500 K, *Chem. Phys. Lett.*, *42*, 466–471.
- Winick, J. R., P. P. Winterstiner, R. H. Picard, D. Esplin, M. G. Mlynczak, J. M. Russell III, and L. L. Gordley (2009), OH layer characteristics during unusual boreal winters of 2004 and 2006, *J. Geophys. Res.*, *114*, A02303, doi:10.1029/2008JA013688.
- Witt, G., J. Rose, and E. J. Llewellyn (1981), The airglow continuum at high latitudes – An estimate of the NO concentration, *J. Geophys. Res.*, *86*, 623–628.

A. L. Alfaro Suzán, W. F. J. Evans, and I. C. McDade, Centre for Research in Earth and Space Science (CRESS) and Department of Earth and Space Science and Engineering (ESSE), York University, 4700 Keele Street, Toronto, ON M3J 1P3, Canada.

P. F. Bernath, Department of Chemistry, University of York, Heslington, York YO10 5DD, UK.

C. D. Boone, Department of Chemistry, University of Waterloo, Waterloo, ON N2L 3G1, Canada.

D. A. Degenstein, R. L. Gattinger, E. J. Llewellyn, and P. Sheese, Department of Physics and Engineering Physics, University of Saskatchewan, Saskatoon, SK S7N 5E2, Canada. (edward.llewellyn@usask.ca)

K. A. Walker, Department of Physics, University of Toronto, Toronto, ON M5S 1A1, Canada.

J.-H. Yee, Johns Hopkins University Applied Physics Laboratory, 11100 Johns Hopkins Rd, Laurel, MD 20723, USA.